nature communications

Article

https://doi.org/10.1038/s41467-025-64780-6

Dual epitaxial telecom spin-photon interfaces with long-lived coherence

Received: 17 February 2025

Accepted: 25 September 2025

Published online: 06 November 2025

Check for updates

Shobhit Gupta[1], Yizhong Huang[2], Shihan Liu[2], Yuxiang Pei[1], Qiang Gao[2], Shuolong Yang[2], Natasha Tomm[3], Richard J. Warburton[3] & Tian Zhong[2]

Optically active solid-state spin qubits thrive as an appealing technology for quantum interconnects and quantum networks, thanks to their atomic size, scalable synthesis, long-lived coherence, and ability to coherently interface with flying qubits. Trivalent erbium dopants, in particular, emerge as an attractive candidate due to their emission in the telecom C band and shielded 4f intra-shell spin and optical transitions. Nevertheless, prevailing top-down architectures for rare-earth qubits and devices have not yet achieved simultaneous long optical and spin coherence, which is necessary for efficient long-distance quantum networks. Here, we demonstrate dual Er^{3+} telecom spin-photon interfaces in two distinct lattice symmetry sites within an epitaxial thin-film platform. By leveraging high matrix crystallinity, controlled proximity of dopants to surfaces, and exploiting host lattice symmetry, we simultaneously achieve kilohertz-level optical linewidth in a strongly symmetry-protected site, and erbium qubit spin coherence times exceeding 10 milliseconds. Additionally, we realize single-shot readout and microwave coherent control of erbium qubits in a fiber-integrated package, enabling rapid deployment and scalability. These advancements highlight the significant potential of high-quality rare-earth qubits and quantum memories assembled using a bottom-up method, paving the way for scalable development of quantum light-matter interfaces tailored for telecommunication quantum networks.

Generation of entanglement over long-distance optical networks[1] serves as the foundation for a broad range of quantum information applications, including secure communication[2], distributed quantum sensing[3], and quantum computation[4]. These applications rely on quantum light-matter interfaces as indispensable building blocks. Such interfaces can potentially be realized using spin qubits in individual atoms with optical transitions, preferably in the low-loss telecommunication bands. Solid-state spin-photon interfaces, such as quantum dots[5,6], defects in diamond[7,8] and silicon carbide[9], T centers[10], and rare-earth ions are among the most promising candidates identified to date. However, few platforms have successfully demonstrated all critical properties simultaneously: long qubit coherence times exceeding a millisecond (necessary for practical networks spanning over 100 km), coherent photon emission with ideally transform-limited linewidths in the telecom C- or O-bands, and scalable device integration that allows efficient channeling of emission into optical fibers. For instance, trivalent erbium dopants in crystals are particularly promising due to their telecom C band emission, and they have been extensively investigated for quantum memories and repeaters[11]. Milliseconds Er spin coherence times[12,13], narrow optical linewidths[14–16], as well as coherent control and readout of single Er spins[17–19] have been demonstrated separately in distinct host crystals and device configurations. However, the ensuing challenge remains to develop a unified Er qubit platform capable of achieving simultaneous long optical and

[1]Department of Physics, University of Chicago, Chicago, IL, USA. [2]Pritzker School of Molecular Engineering, University of Chicago, Chicago, IL, USA. [3]Department of Physics, University of Basel, Basel, Switzerland. e-mail: tzh@uchicago.edu

spin coherence, while allowing for plug-and-play deployment in fiber-optic telecommunication networks.

Engineering designer properties of rare-earth spin-photon interfaces hinges on the precise atomic design, synthesis, and control of the local matrix environment surrounding individual dopants. This is achieved using fundamental principles of symmetry, ligand field theory, and crystal growth techniques. While bulk single crystals[20] exhibit supreme crystalline qualities—as evidenced by record coherence lifetimes in Y_2SiO_5[14,21,22] and $CaWO_4$[12] at cryogenic temperatures—current growth methods inherently limit fine nanoscopic control. Top-down synthesis methods, such as ion implantation[16,23] and photonic integration using bulk or nano-crystals have successfully enabled optical addressing of single ions[24–31], spectral multiplexing[30] and nuclear spin control[32,33]. However, rare-earth dopants embedded in photonic cavities often exhibit varying degrees of degraded coherence compared to their counterparts in bulk crystals. This adverse effect has been attributed to fabrication damage and surface proximity[34], highlighting the need for a redesign of device architectures with the goal of ensuring strong light-matter interactions while maintaining robust coherence[30].

To overcome the limitations of conventional top-down approaches, here we report a rare-earth qubit platform using bottom-up epitaxial growth of Er^{3+} dopants in Y_2O_3 thin film single crystals. This approach showcases excellent matrix crystallinity, precise control of dopants' proximity to surfaces, robust device integrability and scalability. Exploiting two distinct symmetry sites within the Y_2O_3 lattice, we perform both electron spin resonance and optical spectroscopy by coupling Er^{3+} ions to superconducting microwave and fiber-optic microresonators. Site-resolved spin addressing and symmetry protection in one lattice site enable us to engineer erbium qubits with spin coherence exceeding 10 milliseconds and kilohertz-level optical linewidths, achieving single-shot readout with 92% fidelity. These qubits are packaged in a fully fiber-compatible device architecture, offering scalability for network deployment. This advancement represents a substantial step forward in quantum interconnect, providing uncompromised coherence performance for telecommunication quantum networks.

Results

Fiber-integrated Er^{3+} qubit chip

Figure 1 illustrates the schematic of our Er^{3+} qubit device. The die chip consists of a sub-wavelength-thick, cubic-phase Er^{3+} doped Y_2O_3 film, which is transferred onto a distributed Bragg reflector (DBR) stack on a silicon substrate (Methods). High-purity, single crystal Er^{3+}:Y_2O_3 films are epitaxially grown using Molecular Beam Epitaxy (MBE) on silicon (111) wafers[35]. The Er^{3+} dopants are positioned at least 40 nm away from the top and bottom crystal interfaces during the layer-by-layer growth process. Er^{3+} substitutes Y^{3+} in two lattice sites: a C_2 site characterized by both electric and magnetic dipole-allowed $Z_1 \rightarrow Y_1$ optical transitions, and a C_{3i} site, which features only magnetic dipole-allowed optical transitions due to quenched electric dipoles by the centro-inversion symmetry (Fig. 1(a)).

Perpendicular to the plane of the chip, a tunable fiber Fabry-Perot cavity is formed by the DBR substrate and a DBR-coated dimpled fiber[36]. This cavity couples to the 1.5 μm telecom-C band transitions between the lowest crystal field doublets Z_1 and Y_1 of the $^4I_{15/2}$ and $^4I_{13/2}$ spin-orbit levels of Er^{3+}, respectively. When the fiber tip is in rigid contact with the chip[37], the optical cavity achieves the smallest cavity length of $(3/2)\lambda$ (Methods) with measured quality factors ranging from 130,000 to 170,000. A niobium co-planar superconducting microwave resonator, specifically designed with low-impedance to concentrate the magnetic field inside an inductor loop, is patterned on the Y_2O_3 layer. This enables coupling to the microwave electron spin transitions between the Zeeman doublets of the Z_1 optical ground state. The microwave resonator operates at a frequency of 5.81 GHz and achieves a single Er^{3+} spin coupling strength ≥100 Hz. This integrated optical-microwave setup enables spin and optical spectroscopy, as well as coherent control of the Er^{3+} qubits. Combined with the dual symmetry sites of the Er^{3+}, this platform makes possible a comprehensive study of decoherence mechanisms in the epitaxial film matrix by comparing the optical and spin coherence across the two sites to elucidate the underlying electric and magnetic noise.

Er^{3+} spin anisotropy and coherence lifetimes

The intricate interplay between the magnetic anisotropy and the spin coherence for Er spins requires microwave addressing of the spins in a specific symmetry sub-site. To probe the magnetic anisotropy of the Er^{3+} spins, we sweep the magnetic field intensity and the in-plane (XY) field angle θ while detecting the electron spin resonance (ESR) in a sample with Er^{3+} doping at a few parts per million level. Substitutional Er^{3+} ions in the C_2 site occupy six orientationally inequivalent sub-sites with pairs of sub-sites sharing a symmetry axis (principal axis of the g-tensor) along the crystallographic [1,0,0], [0,1,0] and [0,0,1] directions (cuboids in Fig. 2(a)). One sub-site of the C_{3i} site has rotational

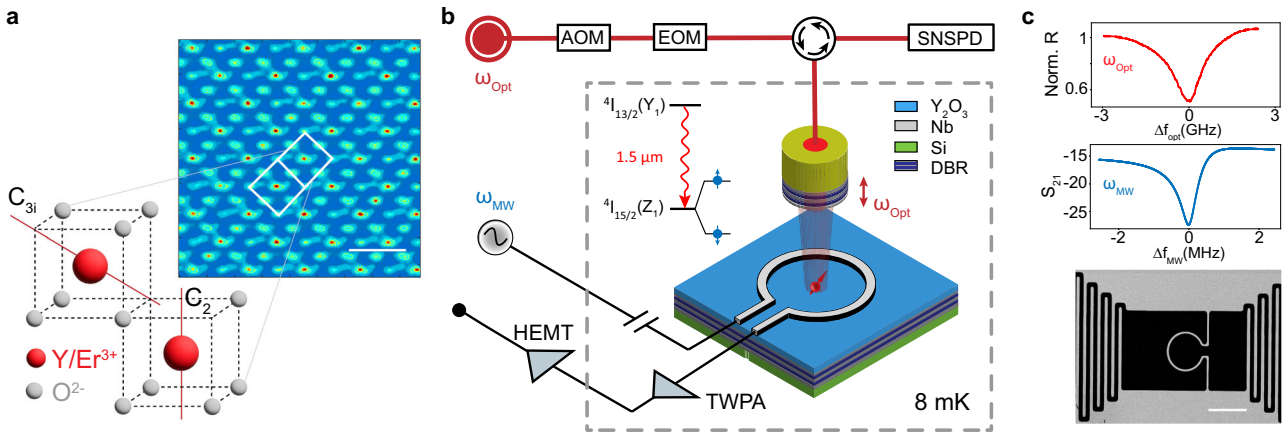

Fig. 1 | Schematic of the Er^{3+} qubit device and experiment setup. a Transmission electron microscope (TEM) lattice image of the cubic-phase epitaxial Y_2O_3 films grown on silicon. The scale bar is 1 nm. Yttrium oxide lattice possesses a C_2 low symmetry and a C_{3i} high symmetry site, with their respective symmetry axes shown in red. **b** The device consists of a tunable cryogenic fiber Fabry-Perot cavity coupled to the $^4I_{15/2}\,Z_1 \rightarrow {}^4I_{13/2}\,Y_1$ optical transition of Er^{3+} and a low-impedance superconducting microwave resonator coupled to the Er^{3+} spin transition at 5–6 GHz. **c** (Top) the reflection spectrum of the fiber Fabry-Perot cavity shows a Q of 139, 000. (Middle) the spectrum of the microwave resonator exhibits a loaded Q of 3000. (Bottom) SEM image of a co-planar superconducting microwave resonator based on niobium. The scale bar is 20 μm. SNSPD superconducting nanowire single photon detector, TWPA traveling wave parametric amplifier, HEMT high electron mobility transistor. DBR distributed Bragg reflector.

https://doi.org/10.1038/s41467-025-64780-6

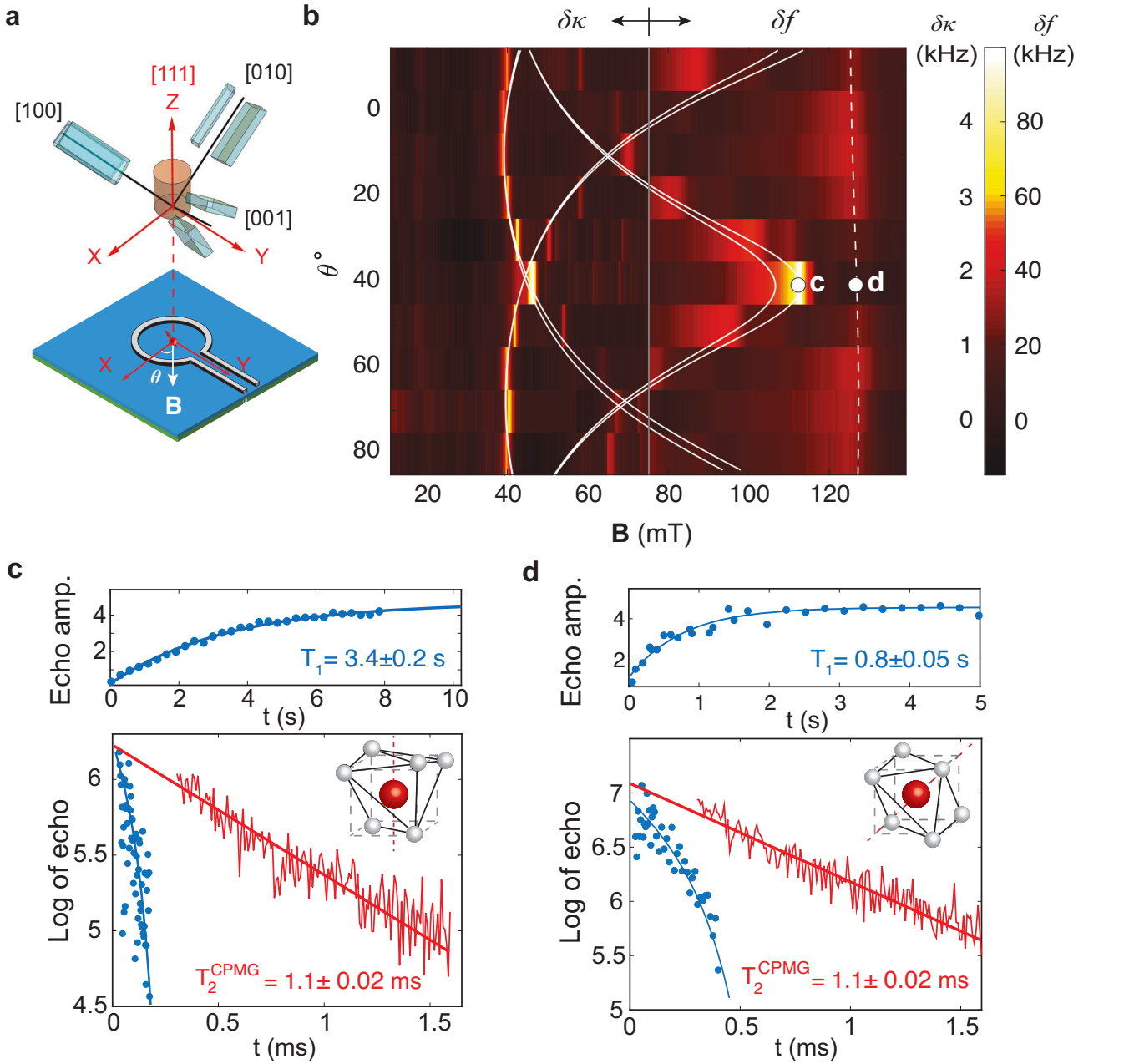

Fig. 2 | Er^{3+} spin anisotropy and coherence lifetimes in single-crystal Y_2O_3 thin films. a Magnetic *g*-tensor axial orientation and anisotropy of six sub-sites of the C_2 symmetry group are represented by cuboids, while one sub-site of the C_{3i} group is represented as a cylinder, with Z axis aligned to the crystallographic [111] direction of Y_2O_3. **b** Scanning the **B** field in the plane of the chip (XY plane) reveals anisotropic (absorptive signal for **B** <75 mT and dispersive signal for **B** >75 mT are stitched) coupling of Er^{3+} in distinct sub-sites to the microwave resonator. White solid and dashed curves are theoretical models for all C_2 and C_{3i} sub-sites. The grey line indicates **B** = 75 mT, where the dispersive and absorptive signals in high and low field ranges are stitched. **c** Spin lifetime (T_1 =3.4 s) (top) and coherence times (bottom) measured with Hahn echo (T_2^{Hahn}=0.18 ms, blue) and Carr-Purcell-Meiboom-Gill (CPMG) sequence (T_2^{CPMG}= 1.11 ms, red) for the C_2 site *g* = 3.6 transition. **d** Spin lifetime (T_1=0.8 s) (top) and coherence times (bottom) measured with Hahn echo (T_2^{Hahn}=0.38 ms, blue) and CPMG sequence (T_2^{CPMG}= 1.1 ms, red) for the C_{3i} site *g* = 3.2 transition. The microwave frequency used for these measurements is 5.81 GHz.

symmetry in the plane of the film (cylinder in Fig. 2(a)). Coupling of Er^{3+} spins in each sub-site results in an absorptive broadening of the resonator linewidth $\delta\kappa$ and a dispersive frequency shift δf by[38]

$$\delta\kappa = \Omega^2\gamma_s/\left(\gamma_s^2+\Delta^2\right) \quad (1)$$

and

$$\delta f = -\Omega^2\Delta/\left(\gamma_s^2+\Delta^2\right), \quad (2)$$

where $\delta\kappa$ is the increase in resonator linewidth, δf is the dispersive resonator frequency shift, Ω is the spin ensemble coupling strength, γ_s is the spin inhomogeneous half-width, and $\Delta = g\mu_B(B - B_0)/\hbar$ where B_0 is the resonance field.

Figure 2(b) plots the absorptive ESR signal for **B** < 75 mT combined with the dispersive signal for **B** ≥75 mT at different in-plane angles θ. Stitching of the two signals is for improved visibility of spin transitions in both field ranges. The full-range data for either absorptive or dispersive signal is presented in Supplementary Fig. 7. We resolve three sets of the C_2 site spin transitions with strong angular

dependence and a C_{3i} site transition with nearly no angular dependence. These features are in reasonable agreement with simulated resonance fields (white solid and dashed curves) calculated from the *g*-tensors of Er^{3+} in Y_2O_3[39], confirming the coupling of Er^{3+} spins. More importantly, the signature anisotropy of all symmetry sites proves the single crystallinity of the Y_2O_3 film over the device area of $50 \times 50\ \mu m^2$. Slight discrepancies in Fig. 2(b) can be attributed to strain-induced perturbation to the *g*-factors (SI Section 1.3). Fitting the ESR signal gives a spin inhomogeneous linewidth of 68 MHz, which is much broader than that in Er^{3+}:$CaWO_4$[12] and is found to be strongly field-angle dependent (SI Section 1.3). Furthermore, we estimate from the dispersive ESR signal a total number of $\approx 6 \times 10^8$ spins in either sub-site that are coupled to the resonator (SI Section 1.2), and a density of Er^{3+} spins of 3.4 parts per million (ppm) for each C_2 sub-site and 3.1 ppm for each C_{3i} sub-site (SI Section 1.2).

Resolved Er^{3+} sub-sites with distinct anisotropy enable us to enhance the qubit coherence times by operating at optimal field configurations. Specifically, spin transitions with lower *g*-factors, thus less noise sensitivity and strongly suppressed noise by a higher field, are preferred[13]. Fixing the magnetic field at $\theta = 40°$ (Fig. 2(b)), we choose a C_2 sub-site with $g = 3.6$ spin transition at 113 mT (circle **c**), and a C_{3i} sub-site with $g = 3.2$ transition at 130 mT (circle **d**), as the target spin qubits. At the calibrated spin temperature < 43.5 mT, the spins in both sites are polarized (SI Section 1.6). The C_2 spins measured a two-pulse Hahn echo spin coherence time T_2^{Hahn} of 0.18 ± 0.01 ms following a stretched exponential decay $e^{-(2t/T_2)^n}$ with a stretch factor $n = 1.18 \pm 0.02$. This indicates spectral diffusion as a source of decoherence[40]. We applied the Carr-Purcell-Meiboom-Gill (CPMG) dynamical decoupling sequence with $N = 500$ π pulses and a pulse separation $2\tau = 8\mu s$ to suppress the spectral diffusion and obtain a T_2^{CPMG} of 1.1 ± 0.02 ms, which is limited by Er-Er spin interactions[41] (SI Section 1.8). Using the more robust XY8 sequence, we obtained a comparable result of $T_2^{\text{XY8}} = 0.9 \pm 0.1$ ms (SI Section 1.8). The C_{3i} spins measured a longer Hahn echo spin coherence time T_2^{Hahn} of 0.38 ± 0.03 ms with a stretch factor $n = 2.11 \pm 0.02$ and T_2^{CPMG} of 1.1 ± 0.02 ms. Temperature dependence of the spin T_2 is also investigated (SI Section 1.6), which reveals the presence of a paramagnetic spin bath contributing to Er^{3+} decoherence at temperatures above ~100 mK. It is worth noting that for Er^{3+} in the C_{3i} site, the ensemble of C_2 site Er^{3+} spins plays the role of a paramagnetic spin bath if they are not polarized.

Long spin relaxation times $T_1 = 3.4 \pm 0.2$ s for the C_2 and 0.8 ± 0.05 s for the C_{3i} sites were measured using saturation recovery sequences, which used a π pulse to first invert the spin population, followed by a Hahn echo measurement. T_1 in both sites shows weak dependence on temperature and spin-cavity frequency detuning, indicating that spin relaxations are not limited by the Purcell effect but dominated by the direct-phonon process with a small contribution from spin flip-flops (SI Section 1.4). In addition, we performed three-pulse stimulated spin echo measurements to reveal spectral diffusion dynamics. The result for Er^{3+} spins in the C_{3i} sub-site indicates a maximum spin linewidth of 2.9 ± 0.5 kHz on a 10 ms timescale (SI Section 1.7).

Using Er^{3+} spins in the C_{3i} site as a probe, we subsequently measure spin relaxation and coherence of multiple sample chips across a Er^{3+}: Y_2O_3 wafer (SI section 1.8). We find a clear trend of increasing spin T_2 lifetimes with decreasing spin spectral density. The longest $T_1 = 1.3 \pm 0.4$ s and Hahn echo $T_2 = 0.47 \pm 0.06$ ms are measured for sample chips near the edge of the wafer, despite a broadened spin inhomogeneous linewdith and thus an increased disorder in the thin film. The corresponding T_2^{CPMG} is 1.72 ± 0.02 ms. These measurements inform that spin T_2 is expected to be enhanced by lowering the Er^{3+} doping density.

Dual Er^{3+} telecom spin-photon interfaces

A quantum spin-photon interface requires a spin-selective, coherent optical transition. Informed by the coherence-optimized magnetic field configurations in the previous ESR measurements, here we demonstrate the optical addressing of individual Er^{3+} spins coupled to a fiber Fabry-Perot cavity (Methods) under identical magnetic field conditions as in Fig. 2(b) points c (**B** = 113 mT) and d (**B** = 130mT). In this experiment, we use a nominally undoped Y_2O_3 epitaxial film, with an estimated Er^{3+} trace concentration of < 50 parts per billion. Figure 3(a) plots typical photoluminescence excitation (PLE) spectra of single Er^{3+} ions in two symmetry sites as the cavity resonance frequency is tuned over the telecom C-band. An ion at 1535.73 nm is found near the center of the C_2 site inhomogeneous line (1535.6 nm), showing a full-width at half-maximum (FWHM) linewidth of 0.4 ± 0.02 MHz. The $g^{(2)}(\tau)$ auto-correlation measurement on this peak confirms single photon emission with $g^{(2)}(0) = 0.025 \pm 0.01$ (right inset) without subtraction of detector dark counts. The non-zero $g^{(2)}(0)$ is attributed to weakly coupled background ions. The optical lifetime of this emitter in the C_2 site was shortened from 8.5 ms to 58 ± 3 μs (Fig. 3(c) inset), giving cavity QED parameters $\{g_0, \kappa, \gamma\} = 2\pi \times \{1\ \text{MHz}, 1.4\ \text{GHz}, 18.7\ \text{Hz}\}$ and a Purcell enhancement of 147 fold (SI Section 2.2). Tuning the cavity to 1545.5 nm, another ion near the center of the C_{3i} site inhomogeneous line (1545.6 nm) shows a significantly narrower PLE linewidth of 71 ± 2 kHz. Due to a weaker coupling strength ($g_0 = 2\pi \times 0.51$ MHz) from a pure magnetic dipole allowed transition (Methods and SI Section 2.2), this Er^{3+} emitter in the C_{3i} site shows a lifetime reduction from 14.6 ms in a bare film to $T_1 = 190 \pm 10$ µs in the cavity. The different Purcell enhancement factors for both sites can be explained by a spatial offset between the cavity electric and magnetic field antinodes. Thus, the ions in two sites are unlikely to have the same overlap with either the cavity electric (for C_2) or magnetic (for C_{3i}) field maxima. Importantly, the stark contrast in two ions' optical linewidths reveals a significant role of symmetry in their optical coherence: while both emitters experience dephasing by coupling to a common magnetic noise bath, the C_{3i} emitter is protected from first-order coupling to electric noise due to a quenched permanent electric dipole.

Furthermore, a high system photon detection efficiency of 6.4% (3.9%) for the Er^{3+} emission in the C_2 (C_{3i}) sites (SI Section 2.1) enables single-shot optical readout of both qubits. First, we verify that these ions have the desired spin frequencies by screening their optical frequency shifts with **B** field strength to extract $|g_e - g_g|$, and by confirming their ground-state g_g factors from spin Rabi oscillations using a microwave drive (Supplementary Fig. 3). The branching ratios and cyclicities of the respective Er^{3+} optical transitions are measured to be ~480 and > 1000 for the C_2 and C_{3i} sub-sites, respectively (SI Section 2.4). At the calibrated spin temperature (SI Section 1.6), both Er^{3+} spins are thermally initialized to the $|\downarrow\rangle$ state with near unit spin polarization, and we used optical pumping to initialize the C_2 site Er^{3+} to the $|\uparrow\rangle$ spin state. For the C_{3i} site Er^{3+}, optical pumping is difficult due to the very high cyclicity. Hence, we used a microwave π pulse to invert the spin to $|\uparrow\rangle$ for characterizing the readout fidelity. A histogram of photon counts during the readout using 100 optical pulses each with a 0.3 ms-interval for the Er^{3+} qubit in the C_2 site, is shown in the left inset of Fig. 3(a). The average photon number is 6.2 (0.05) for the $|\downarrow\rangle$ ($|\uparrow\rangle$) state. This leads to an average readout fidelity of 97.0 ± 0.5 % using 1 photon threshold. The average readout fidelity for the C_{3i} Er^{3+} ion is 91.8 ± 0.5 % (Supplementary Fig. 1). The lower fidelity in the latter is primarily due to a faster spin relaxation ($T_1 = 1.6$ s) during the repeated readout pulses for the C_{3i} site.

Probing optical coherence of ions in two symmetry sites within a common lattice elucidates crucial dynamics of optical spectral diffusion. We first focus on the C_2 site emitter. For long-term spectral stability, we repeated PLE scans for an Er^{3+} ion over ≈ 10 hours (Fig. 3(b)). The central peak of the PLE spectrum shows a root-mean-square (rms) variation $\ll 1$ MHz, attesting to the absence of a significant long-term drift. Nevertheless, the sub-MHz-wide PLE indicates a broadening mechanism occuring on a much shorter timescale. Typically, three-pulse photon echo technique is used to measure the spectral diffusion

https://doi.org/10.1038/s41467-025-64780-6

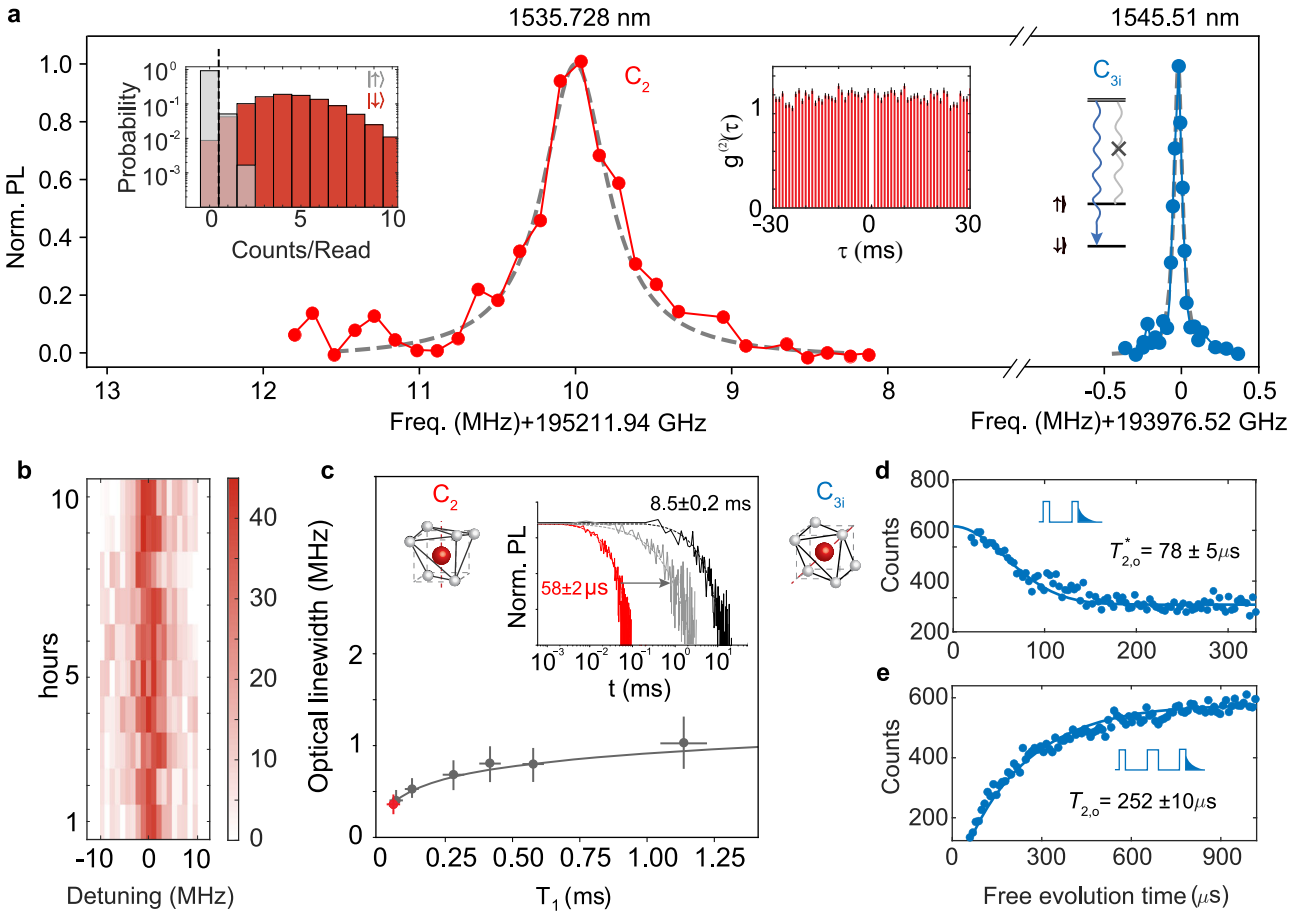

Fig. 3 | Dual Er^{3+} spin-photon interfaces and optical coherence. a Narrow photoluminescence excitation spectrum is observed from single Er^{3+} ions in the C_2 (**B** = 113 mT) and C_{3i} (**B** = 130 mT) sites of Y_2O_3. (Right inset) $g^{(2)}$ auto-correlation measurement for an Er^{3+} ion in the C_2 site shows $g^{(2)}(0)$= 0.025. (Left inset) Histogram of photon counts during a 100-pulse readout for an ion in the C_2 site. **b** Long-term spectral stability of an Er^{3+} emitter in the C_2 site. **c** Short-term optical spectral diffusion of Er^{3+} in the C_2 site as optical T_1 lifetime is tuned. Inset shows the tuning of Purcell enhancement. Grey line indicates the fit to a spectral diffusion model with a dominant logarithmic component. **d** Optical Ramsey ($\pi/2 - \pi/2$) measurement for an Er^{3+} ion in the C_{3i} site. **e**. Optical T_2 measured by ($\pi/2 - \pi - \pi/2$) photon echo for the same ion in (**d**). Results for additional optical measurements on the single Er^{3+} ion in the C_2 site are presented in the Supplementary Fig. 1 and Supplementary Fig. 2.

dynamics on the time scale of the emitter's optical lifetime. Here, by taking advantage of in-situ tuning of the Purcell factor (SI Section 2.3), we probe the similar dynamics by sweeping the cavity-emitter detuning to reveal a broadening of the Er^{3+} PLE linewidth over a millisecond temporal window. Without an applied magnetic field, the PLE linewidth is ≈ 1 MHz. A modest **B** field (≥110 mT) freezes the magnetic noise, leading to a reduced linewidth of 0.4 MHz, which then noticeably increases as the emitter T_1 lifetime is slowed from 58 μs to 1.1 ms (gray data in Fig. 3(c)). This temporal evolution of optical spectral diffusion can be modeled based on frozen paramagnetic spin baths[14] plus a fast (≪50 μs) spectral diffusion process by non-magnetic noise (grey curve in Fig. 3(c)) (SI Section 2.5). The latter is likely related to fluctuating electric-dipoles from tunneling two-level-systems (TLS) that are evidenced in separate ESR measurements (SI Section 1.9). We then measured the optical $T_{2,o}$ coherence time of this emitter in the C_2 site using a $\pi/2$-π-$\pi/2$ photon echo sequence, as shown in Supplementary Fig. 2. A single exponential fit gives $T_{2,o}$ = 67 ± 3 μs, corresponding to a homogeneous linewidth of $1/\pi T_{2,o}$ = 4.8 ± 0.2 kHz. This linewidth is about two orders of magnitude narrower than the PLE linewidth, indicating that most dephasing is rephased by the echo sequence and providing further evidence for fast fluctuating noise on a short timescale.

Next, we turn to the inversion-symmetric C_{3i} site. With the magnetic field configured as in point d in Fig. 2(b), the excited ($g_e \approx 0$) and ground state (g_g=3.2) g-factors of Er^{3+} result in a correlated spin and optical coherence that is primarily limited by the magnetic noise. We find that the measured PLE linewidth in the C_{3i} site, while already narrow (71 kHz in Fig. 3(a)), is strongly dependent on the optical Rabi frequency used to excite the ion[42], and thus does not inform accurately the intrinsic optical linewidth of the emitter. To obtain the optical coherence, we performed optical Ramsey measurement on the Er^{3+} ion, using two optical $\pi/2$ pulses with an optical Rabi frequency of $2\pi \times 50$ kHz (corresponding to a cavity mean photon number of 0.01). The measured $T^*_{2,o}$ using a stretched exponential fit is 78 ± 5 μs with a stretch factor of 2.1 ± 0.1, leading to a pure optical dephasing rate of 3.2 ± 0.3 kHz after subtracting the radiative rate of $1/2\pi T_1$ = 0.83 kHz. This is in good agreement with the magnetic-noise limited spin spectral diffusion linewidth discussed previously (and SI Section 1.7), thus indicating an effective inversion-symmetry protection against fluctuating electric noise, inferring a minimally distorted lattice site. It is worth noting that such a long optical coherence is only observed with a weak Rabi drive frequency. Ramsey measurement with higher ($> 2\pi \times 1$ MHz) Rabi frequency resulted in diminished optical coherence, indicating instantaneous spectral diffusion or spurious excitation of other lattice defects in the Y_2O_3 thin film. Additionally, we measured the optical $T_{2,o}$ = 252 ± 10 μs using photon echo sequence and a single exponential fit (Fig. 3(e)). This value approaches the long optical coherence times observed in bulk Er^{3+}:Y_2O_3 polycrystals at a similar temperature[15].

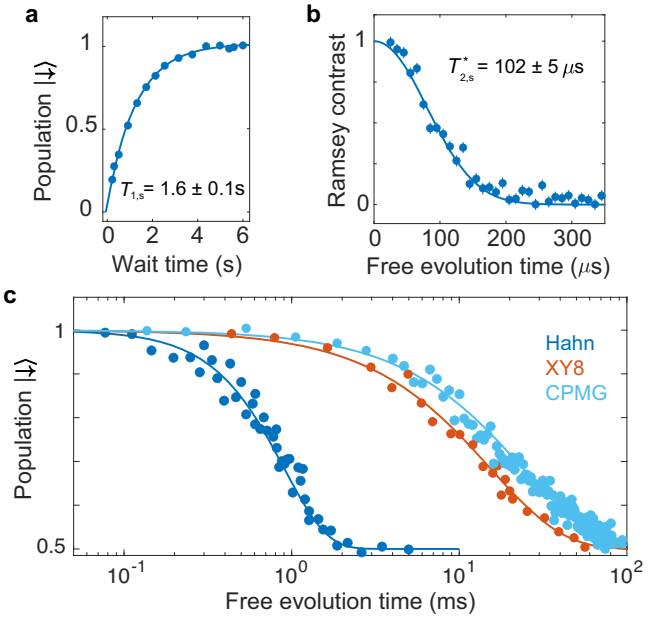

Fig. 4 | Er^{3+} spin qubit coherence in the C_{3i} site. a Spin lifetime measured by a π inversion pulse followed by delayed optical readout. **b** Spin Ramsey coherence. The fringe contrast is extracted from the normalized readout signal difference when alternating between a 0 and π phase of the second $\pi/2$ pulse. A fit to $e^{-(t/T^*_{2,s})^n}$ yields a $T^*_{2,s}$ = 102 ± 5 μs with n = 2.1 ± 0.1. The error bars represent one standard deviation. **c** Hahn echo $T_{2,s}$, XY8 and CPMG dynamically decoupled spin coherence for the Er^{3+} ion in the C_{3i} site. For the CPMG measurement, the π pulse separation is fixed at 8 μs. The plot shows the CPMG readout with increasing number of refocusing pulses. The applied magnetic field is 130 mT.

Last, we apply microwave control and optical readout to the C_{3i} Er^{3+} spin-photon interface. The microwave drive is tuned to the exact spin resonance frequency (5.8 GHz) and the optimal pulse length (Method). Spin T_1 was measured to be 1.6 ± 0.1 s using an inversion pulse followed by delayed optical readout. Ramsey sequence measured a $T^*_{2,s}$ = 102 ± 5 μs with a stretch factor of 2.1, further substantiating the kHz spin linewidth. Spin coherence by Hahn echo, XY8 and CPMG dynamical decoupling sequences are plotted in Fig. 4(c). A Hahn echo $T_{2,s}$ = 0.85 ± 0.5 ms was obtained, which is longer than that in the ESR ensemble measurement in the sample with a higher doping concentration. This improvement of spin coherence is attributed to the significantly reduced spin density, which results in a weaker Er-Er dipolar interaction and a possibly reduced paramagnetic spin bath. An XY8 dynamical decoupling sequence allowed coherence to be extended to 15 ± 1 ms. Meanwhile, CPMG sequence with a fixed π pulse interval of 8 μs led to a coherence time up to 24 ± 1 ms with increasing number of π pulses. Both XY8 and CPMG sequences demonstrate single spin coherence times that are over 10-fold longer than those observed in higher density spin ensembles (Fig. 2(d)). This affirms that Er–Er dipolar interactions are the primary limitation of spin coherence in the previous ensemble measurements, and likely remain so in the measured single spin coherence.

Discussion

An optical dephasing rate on the order of a few kilohertz for Er^{3+} spin qubits in the C_{3i} site is among the longest optical coherences reported for single Er^{3+} dopants[18,30] and approches the ensemble-averaged Er^{3+} optical homogeneous linewidth observed in polycrystalline Y_2O_3 ceramics[15] and other prominent rare-earth doped bulk single crystals[20]. The measured single Er^{3+} spin coherence time is more than an order of magnitude longer than that observed in $CaWO_4$[18] and Si-on-insulator (SOI) hosts[19], as well as the ^{171}Yb clock qubit in YVO_4[43]. In all the latter three cases, single ions are incorporated into photonic crystal cavities. Combined with > 10 millisecond dynamically decoupled spin coherence, we showcase a telecom-band spin-photon interface synthesized using a bottom-up approach and fully fiber-integrated for plug-and-play deployment in a quantum network. While the current optical dephasing parameters ($T^*_2/2T_1$=0.2, $T_2/2T_1$=0.67) do not reach the fully transform-limited linewidth, they compare favorably with those reported for single Er^{3+} in $CaWO_4$ ($T^*_2/2T_1$=0.12, $T_2/2T_1$=0.56)[18] and in SOI ($T^*_2/2T_1 < 0.01$)[19]. These parameters are sufficient to enable remote spin entanglement generation via post-selection protocols[7]. Realistic improvement to the fiber cavity finesse (× 1.4) and mode alignment of atomic dipoles (× 2) will lead to a cavity-QED regime of $\{g_0, \kappa, \gamma_h\} = 2\pi \times \{1\,\text{MHz}, 1\,\text{GHz}, 4\,\text{kHz}\}$, achieving a unit single-ion cooperativity and fully indistinguishable emission. For even stronger coupling, a slot-mode Y_2O_3 on silicon-on-insulator photonic resonators similar to[44] can potentially offer another order-of-magnitude higher cooperativity without degrading Er^{3+} optical coherence. Such enhancements will facilitate faster single-shot spin readout and better photon indistinguishability than current work, which will enable Er^{3+}-Er^{3+} remote entanglement, single Er-photon gate[45] and non-destructive detection of telecom photons[46]. For further outlook, the strong dipolar coupling between Er^{3+} pairs from the same symmetry site[47] or between dual sites (C_2-C_{3i}) can realize decoherence-protected singlet-triplet qubits[48], two-qubit entanglement and logic gates[49]. If a pair of Er^{3+} can be deterministically placed in the nearby C_2 and C_{3i} sites, they may combine the long coherence times of the C_{3i} site with fast optical control and readout offered by the C_2 site.

The measured single Er^{3+} spin $T_{2,s}$ and dynamically-decoupled $T^{DD}_{2,s}$ are similar to the spin ensemble coherence observed in polycrystalline Y_2O_3 ceramics[13], with $T_{2,s}$ of the same order of magnitude and $T^{DD}_{2,s}$ exceeding by one order of magnitude the record values previously reported for a single Er^{3+} spin in $CaWO_4$[50]. We note that the experiment in ref.[50] used solely microwave measurements without involving optical addressing, and their spin coherence is limited by their Purcell-enhanced $T_{1,s}$. As evident from the microwave ESR measurements, the current spin coherence is expected to remain limited by the Er-Er dipolar interactions. Therefore, the single Er^{3+} spin coherence time can potentially be further improved by lowering the trace Er concentration via an improved MBE growth of ultra-pure Y_2O_3 films. Isolating an $^{167}Er^{3+}$ ion in Y_2O_3 and exploiting the available zero first-order Zeeman (ZEFOZ) transitions in this material[39] also provides a pathway towards ultra-long Er^{3+} coherence. Following the first demonstration of the epitaxial rare-earth qubit platform, ensuing improvements in the thin film material quality are anticipated: hybrid oxide growth methods combining MBE and Chemical Vapor Deposition (CVD)[51,52] may produce a matrix with reduced paramagnetic impurities or charge-trapping defects (e.g. F^+ centers); co-doping Er with other rare-earth elements that serve as charge-trapping centers[53] could stabilize the local charge configuration and reduce optical spectral diffusion, especially for Er^{3+} ions in the C_2 site. Finally, the thin film platform is amenable to integration with hybrid quantum degrees of freedom, such as coupling Er^{3+} to surface acoustic wave or suspended opto-mechanical resonators, where strong confinement of phonons allows for localized spin manipulations. Lithographically patterned Er^{3+} doped films conforming to the overlapping modes of optical and microwave cavities can considerably boost microwave-to-optical quantum transduction efficiency[54].

Methods

Y_2O_3 thin-film growth and integration

Yttrium oxide (Y_2O_3) has a cubic crystal structure (T^7_h space group) with 16 formula units per unit cell. These 32 Y^{3+} sites can be grouped into two classes with 24 sites of C_2 point group symmetry and 8 sites of C_{3i} point group symmetry (Fig. 1(a)), where each of the 32 yttrium (Y^{3+}) ions in a unit cell can be substituted with an Er^{3+} ion with equal probability.

Er^{3+}-doped Y_2O_3 thin-films were grown epitaxially on silicon (111) wafers using molecular beam epitaxy[35] technique, thanks to a small lattice mismatch between Y_2O_3(222) and Si(111) planes. The MBE growth used 5N (i.e. ≥99.999%) high purity yttrium and erbium metal sources, and was performed at temperatures between 600 and 920 °C and monitored in-situ during growth using Reflection High-Energy Electron Diffraction (RHEED). The doped films for the ESR spectroscopy have a thickness of 1.4 μm and feature a doping profile with a 40 nm undoped buffer layer at both the top surface and the bottom Y_2O_3/Si interface. A nominally undoped film, produced using the same growth process, is used for the fiber-integrated qubit chip. All samples were annealed in air at 600 °C for 1 hour prior to device assembly and fabrication.

To integrate the Y_2O_3 film onto a DBR mirror substrate, the thin-film sample and the DBR substrate are diced into 10 × 10 mm chips and put in hot N-Methylpyrrolidone (NMP) for > 5 hours for cleaning. The Y_2O_3 chip is then bonded on the DBR mirror using HSQ e-Beam resist as an adhesive layer by pressing them together with a home-built clamp and baked on a hot plate at 250 °C for 1 hour. The samples are then removed from the clamp and annealed in a rapid thermal processing (RTP) tool at 600/500 °C in air for 1 hour, which turns the HSQ to thermally stable oxide. Following a successful bonding, the back silicon handle is removed by reactive ion etching. A spacer layer of Si_3N_4 was deposited on the chip to planarize it and adjust the device thickness as needed.

Superconducting microwave resonator and measurement setup

The co-planar superconducting resonator has a design impedance of 9.4 Ω, with simulated capacitance ≈ 2.8-3.2 pF and inductance $L = 1/4\pi^2\omega^2 C \approx 260$ pH. The resonator frequency was tuned in 5.5-5.9 GHz by varying the width and spacing of the inter-digitated finger (IDF) capacitor in the range of 3.3–3.5 μm. The stray inductance from the capacitor was ≈ 200 pH, and the inductor loop has a diameter 20 μm and an inductance ≈ 60 pH. For measurements only involving microwave electron spin resonance (ESR), we adopt a flip-chip mounting technique for high-throughput sample characterization. The resonators were patterned either on a high-resistivity silicon substrate or on the Y_2O_3 films following a recipe described in SI Section 1.1. The devices including the microwave resonator, were mounted on the 8 milliKelvin stage of a Bluefors LD-250 dilution refrigerator, and a 3-axis vector magnet (AMI 430) was used to apply a magnetic field in-plane of the resonator. The device used in Fig. 2 had a frequency of 5.81 GHz, intrinsic Q ≈ 370,000, and external Q ≈ 3000. The resonators showed varying degrees of asymmetric lineshape as seen in Fig. 1(c) due to reflections from imperfect impedance matching in the transmission line. Continuous-wave ESR measurements were performed using a vector network analyzer with -80 dBm on-chip power. The pulsed ESR measurements used a low noise amplifier chain comprising a Josephson traveling wave parametric amplifier (TWPA) at the 8 mK stage, a low noise amplifier at 4 Kelvin, and room temperature electronics for high sensitivity spin echo detection. For microwave control of the Er^{3+} qubit in Fig. 4, a coplanar waveguide as in Fig. 1(b) is patterned on the Y_2O_3 film and is solely used to deliver the microwave drive to the spin qubit. Neither a microwave resonator nor the readout amplifier chain was used. The exact microwave frequency and pulse width are determined by optimizing the spin Rabi oscillations detected via optical readout (Supplementary Fig. 3). Complete details of the setup are included in SI Section 1.1 and Supplementary Fig. 4.

Cryogenic tunable fiber cavity and optical measurement setup

The dimpled fiber mirror was prepared by creating a concave depression using CO_2 laser ablation as described in[36]. Following the convention in[36], our fiber dimple had a radius of curvature R of 40 μm, a depth t of 1.54 μm, and a structure diameter d of 10.35 μm. The fiber dimple was subsequently coated with the DBR mirror stack similar to that on the substrate, which has a nominal transmission of 50 ppm on the fiber and 10 ppm on the substrate. The theoretical cavity finesse is 105,000.

The fiber mirror is mounted in a fiber chuck and secured with thin copper shims. The fiber tip and the device chip are brought into a rigid contact using a piezoelectric nanopositioner to form a stable, small ($L = 3/2\lambda$) Fabry-Perot cavity without active stabilization. The fiber mirror showed a one-way reflection of ≈ 80%, which included transmission through the mirror coating and loss due to a mismatch between the cavity and the fiber mode. Even after establishing rigid contact, the optical cavity resonance is still coarsely tunable by up to 40 nm in wavelengths at cryogenic temperatures by stepping the nanopositioner. At the same time, continuous fine-tuning at a rate of 1.3 GHz/V over 80 GHz is achieved by adjusting the piezo voltage. The measured finesse of an empty cavity (no Y_2O_3 layer) ranges from 40,000 to 60,000 over the tunable wavelengths. Optical measurements on the C_2 site were performed in the cavity with a finesse of 46,300 (Q = 139,000), while on the C_{3i} site, the cavity finesse was 50,300 (Q = 151,000). Furthermore, based on the change in cavity finesse with and without the Y_2O_3 film, we calculate an upper bound on the optical absorption of the Y_2O_3 thin film to be 1.8 dB/m, indicating outstanding optical quality. A slight asymmetry of the fiber cavity reflection spectrum in Fig. 1(c) is attributed to the Fano effect and can be minimized by adjusting the polarization of the excitation laser. Some cavities showed a fundamental cavity mode that is splitted into two orthogonal linear polarization modes, as previously reported in fiber cavities[37,55]. The fiber cavity used for the measurements in Figs. 3-4 showed polarization mode splitting by 30 GHz.

The optical setup comprises three acousto-optic modulators (AOM) in series for generating pulses with a high extinction ratio of 160 dB and an electro-optic modulator (EOM) for a fine frequency sweep of the laser. Photoluminescence from Er^{3+} was detected by a superconducting nanowire single photon detector (SNSPD) with ≈ 70% detection efficiency and a negligible (< 0.1 Hz) dark count rate. The near-zero dark count rate was achieved using a cryogenic fiber band pass filter mounted at the 50 K stage in the same fridge where the SNSPD is mounted. The laser was locked to a UHV stable reference cavity with short-term laser linewidth of 400 Hz and a long-term drift <100 kHz/day. The laser power on-chip is actively stabilized via variable optical attenuators.

Selection rules for Er^{3+} optical transitions in the C_{3i} site

Optical transitions of rare-earth dopants in the sites with inversion symmetry are allowed only as magnetic dipole transitions and are governed by the selection rule: $\Delta J \leq 1$ and $\Delta M_J \leq 1$. For the C_{3i} site Er^{3+} optical transitions, the wavefunctions of the lowest crystal-field doublet Z_1 of $^4I_{15/2}$ and Y_1 of $^4I_{13/2}$ are expected to be dominated by $M_J = \pm 15/2$ and $M_J = \pm 13/2$ components, respectively. Therefore, spin-flipping optical transitions between the Kramer double groups of Z_1 and Y_1 are largely forbidden due to a large change in $\Delta M_J \gg 1$. To verify this, we measured cumulative photoluminescence after repeated pulsed excitations on the C_{3i} ions, which demonstrated high cyclicity (> 1000) and a negligible branching ratio for the spin-flipping transitions (SI Section 2.4, which also includes cyclicity measurement for the C_2 site). We note that the significant cavity enhancement and the narrow cavity linewidth (1.3 GHz) relative to the spin frequency also contribute to this high cyclicity.

Data availability

The data that support the findings of this study are available from the corresponding author upon request.

References

1. Kimble, H. J. The quantum internet. *Nature* **453**, 1023–1030 (2008).

2. Pirandola, S. et al. Advances in quantum cryptography. *Adv. Opt. Photon.* **12**, 1012–1236 (2020).
3. Proctor, T. J., Knott, P. A. & Dunningham, J. A. Multiparameter estimation in networked quantum sensors. *Phys. Rev. Lett.* **120**, 080501 (2018).
4. Cacciapuoti, A. S. et al. Quantum internet: networking challenges in distributed quantum computing. *IEEE Network* **34**, 137–143 (2020).
5. De Greve, K. et al. Quantum-dot spin–photon entanglement via frequency downconversion to telecom wavelength. *Nature* **491**, 421–425 (2012).
6. Delteil, A. et al. Generation of heralded entanglement between distant hole spins. *Nat. Phys.* **12**, 218–223 (2016).
7. Bernien, H. et al. Heralded entanglement between solid-state qubits separated by three metres. *Nature* **497**, 86–90 (2013).
8. Stas, P.-J. et al. Robust multi-qubit quantum network node with integrated error detection. *Science* **378**, 557–560 (2022).
9. Anderson, C. P. et al. Five-second coherence of a single spin with single-shot readout in silicon carbide. *Sci. Adv.* **8**, eabm5912 (2022).
10. Higginbottom, D. B. et al. Optical observation of single spins in silicon. *Nature* **607**, 266–270 (2022).
11. Kimiaee Asadi, F. et al. Quantum repeaters with individual rare-earth ions at telecommunication wavelengths. *Quantum* **2**, 93 (2018).
12. Dantec, M. L. et al. Twenty-three-millisecond electron spin coherence of erbium ions in a natural-abundance crystal. *Sci. Adv.* **7**, eabj9786 (2021).
13. Gupta, S., Wu, X., Zhang, H., Yang, J. & Zhong, T. Robust millisecond coherence times of erbium electron spins. *Phys. Rev. Appl.* **19**, 044029 (2023).
14. Böttger, T., Thiel, C. W., Sun, Y. & Cone, R. L. Optical decoherence and spectral diffusion at 1.5μm in Er^{3+}:Y_2SiO_5 versus magnetic field, temperature, and Er^{3+} concentration. *Phys. Rev. B* **73**, 075101 (2006).
15. Fukumori, R., Huang, Y., Yang, J., Zhang, H. & Zhong, T. Subkilohertz optical homogeneous linewidth and dephasing mechanisms in Er^{3+}:Y_2O_3 ceramics. *Phys. Rev. B* **101**, 214202 (2020).
16. Gritsch, A., Weiss, L., Früh, J., Rinner, S. & Reiserer, A. Narrow optical transitions in erbium-implanted silicon waveguides. *Phys. Rev. X* **12**, 041009 (2022).
17. Raha, M. et al. Optical quantum nondemolition measurement of a single rare earth ion qubit. *Nat. Commun.* **11**, 1605 (2020).
18. Ourari, S. et al. Indistinguishable telecom band photons from a single Er ion in the solid state. *Nature* **620**, 977–981 (2023).
19. Gritsch, A., Ulanowski, A., Pforr, J. & Reiserer, A. Optical single-shot readout of spin qubits in silicon. *Nat. Commun.* **16**, 64 (2025).
20. Thiel, C., Böttger, T. & Cone, R. Rare-earth-doped materials for applications in quantum information storage and signal processing. *J. Lumin.* **131**, 353–361 (2011).
21. Ortu, A. et al. Simultaneous coherence enhancement of optical and microwave transitions in solid-state electronic spins. *Nat. Mater.* **17**, 671–675 (2018).
22. Rančić, M., Hedges, M. P., Ahlefeldt, R. L. & Sellars, M. J. Coherence time of over a second in a telecom-compatible quantum memory storage material. *Nat. Phys.* **14**, 50–54 (2018).
23. Berkman, I. R. et al. Observing Er^{3+} sites in si with an in situ single-photon detector. *Phys. Rev. Appl.* **19**, 014037 (2023).
24. Zhong, T. et al. Optically addressing single rare-earth ions in a nanophotonic cavity. *Phys. Rev. Lett.* **121**, 183603 (2018).
25. Dibos, A. M., Raha, M., Phenicie, C. M. & Thompson, J. D. Atomic source of single photons in the telecom band. *Phys. Rev. Lett.* **120**, 243601 (2018).
26. Yu, Y. et al. Frequency tunable, cavity-enhanced single erbium quantum emitter in the telecom band. *Phys. Rev. Lett.* **131**, 170801 (2023).
27. Xia, K. et al. Tunable microcavities coupled to rare-earth quantum emitters. *Optica* **9**, 445–450 (2022).
28. Huang, J.-Y. et al. Stark tuning of telecom single-photon emitters based on a single Er^{3+}. *Chinese Phys. Lett.* **40**, 070301 (2023).
29. Yang, L., Wang, S., Shen, M., Xie, J. & Tang, H. X. Controlling single rare earth ion emission in an electro-optical nanocavity. *Nat. Commun.* **14**, 1718 (2023).
30. Ulanowski, A., Merkel, B. & Reiserer, A. Spectral multiplexing of telecom emitters with stable transition frequency. *Sci. Adv.* **8**, eabo4538 (2022).
31. Deshmukh, C. et al. Detection of single ions in a nanoparticle coupled to a fiber cavity. *Optica* **10**, 1339–1344 (2023).
32. Ruskuc, A., Wu, C.-J., Rochman, J., Choi, J. & Faraon, A. Nuclear spin-wave quantum register for a solid-state qubit. *Nature* **602**, 408–413 (2022).
33. Uysal, M. T. et al. Coherent control of a nuclear spin via interactions with a rare-earth ion in the solid state. *PRX Quantum* **4**, 010323 (2023).
34. Wu, C.-J. et al. Near-infrared hybrid quantum photonic interface for $^{171}Yb^{3+}$ solid-state qubits. *Phys. Rev. Appl.* **20**, 044018 (2023).
35. Singh, M. K. et al. Epitaxial Er-doped Y_2O_3 on silicon for quantum coherent devices. *APL Mater.* **8**, 031111 (2020).
36. Hunger, D., Deutsch, C., Barbour, R. J., Warburton, R. J. & Reichel, J. Laser micro-fabrication of concave, low-roughness features in silica. *AIP Adv.* **2**, 012119 (2012).
37. Najer, D. et al. A gated quantum dot strongly coupled to an optical microcavity. *Nature* **575**, 622–627 (2019).
38. Dold, G. et al. High-cooperativity coupling of a rare-earth spin ensemble to a superconducting resonator using yttrium orthosilicate as a substrate. *Phys. Rev. Appl.* **11**, 054082 (2019).
39. Rajh, T. et al. Hyperfine interactions and coherent spin dynamics of isotopically purified $^{167}Er^{3+}$ in polycrystalline Y_2O_3. *Mater. Quantum Technol.* **2**, 045002 (2022).
40. Mims, W. B., Nassau, K. & McGee, J. D. Spectral diffusion in electron resonance lines. *Phys. Rev.* **123**, 2059–2069 (1961).
41. Harbridge, J. R., Eaton, S. S. & Eaton, G. R. Comparison of electron spin relaxation times measured by carr–purcell–meiboom–gill and two-pulse spin-echo sequences. *J. Magn. Reson.* **164**, 44–53 (2003).
42. DeVoe, R. G. & Brewer, R. G. Experimental test of the optical Bloch equations for solids. *Phys. Rev. Lett.* **50**, 1269–1272 (1983).
43. Kindem, J. M. et al. Control and single-shot readout of an ion embedded in a nanophotonic cavity. *Nature* **580**, 201–204 (2020).
44. Xu, X. et al. Epitaxial single-crystal rare-earth oxide in horizontal slot waveguide for silicon-based integrated active photonic devices. *Opt. Express* **28**, 14448–14460 (2020).
45. Reiserer, A., Kalb, N., Rempe, G. & Ritter, S. A quantum gate between a flying optical photon and a single trapped atom. *Nature* **508**, 237–240 (2014).
46. O'Brien, C., Zhong, T., Faraon, A. & Simon, C. Nondestructive photon detection using a single rare-earth ion coupled to a photonic cavity. *Phys. Rev. A* **94**, 043807 (2016).
47. Hu, G. et al. Single site optical spectroscopy of coupled Er^{3+} ion pairs in silicon. *Quantum Sci. Technol.* **7**, 025019 (2022).
48. Laplane, C., Zambrini Cruzeiro, E., Fröwis, F., Goldner, P. & Afzelius, M. High-precision measurement of the Dzyaloshinsky-Moriya interaction between two rare-earth ions in a solid. *Phys. Rev. Lett.* **117**, 037203 (2016).
49. Asadi, F. K., Wein, S. C. & Simon, C. Protocols for long-distance quantum communication with single ^{167}Er ions. *Quantum Sci. Technol.* **5**, 045015 (2020).
50. Wang, Z. et al. Single-electron spin resonance detection by microwave photon counting. *Nature* **619**, 276–281 (2023).
51. Harada, N. et al. Chemically vapor deposited Eu^{3+}:Y_2O_3 thin films as a material platform for quantum technologies. *J. Appl. Phys.* **128**, 055304 (2020).

52. Blin, A. et al. Erbium-doped yttrium oxide thin films grown by chemical vapor deposition for quantum technologies. *Appl. Phys. Rev.* **12**, 011421 (2025).
53. Liao, C. et al. Electron trapping optical storage using a single-wavelength light source for both information write-in and read-out. *Laser Photonics Rev.* **17**, 2300016 (2023).
54. Williamson, L. A., Chen, Y.-H. & Longdell, J. J. Magneto-optic modulator with unit quantum efficiency. *Phys. Rev. Lett.* **113**, 203601 (2014).
55. Tomm, N. et al. A bright and fast source of coherent single photons. *Nat. Nanotechnol.* **16**, 399–403 (2021).

Acknowledgements

We thank David I. Schuster and Tanay Roy for their help on the ESR microwave experiment. We acknowledge Matvey Schmukler, Haechan An, Hal Owens, Andrew Kamen, Xiaoyang Liu, Chao-Fan Wang for their technical assistance. We thank Woojoo Lee for help setting up the oxide MBE facility at the University of Chicago, and Michael Flatte, Alexey Lyasota and Ian Berkman for the discussion on coherence spectroscopy. We acknowledge MIT Lincoln Laboratory for providing the Josephson traveling-wave parametric amplifier (TWPA) and Argonne National Laboratory for the initial thin film growth. We thank Matthew Shaw for providing the single photon nanowire superconducting detectors. The work by Y.H., S.L., Y.P., Q.G., S.-L.Y., T.Z. was funded by a National Science Foundation (NSF) Faculty Early Career Development Program (CAREER) grant 1944715 and Army Research Office (ARO) grant W911NF2010296. S.G. was primarily supported by the University of Chicago Materials Research Science and Engineering Center, which is funded by NSF under award number DMR-2011854. N.T. and R.J.W. were funded by NCCR QSIT and by the Swiss National Science Foundation project 200020_204069. Equipment funding was provided by the Department of Defense Office of Naval Research (N00014-22-1-2281) and the Department of Energy QNEXT quantum science and engineering research center.

Author contributions

S.G., Y.H. and S.L. fabricated devices for this study. S.G., Y.H., S.L., Y.P. and T.Z. performed the experiments and analysed the data. Q.G. and S.-L.Y. grew the undoped thin film samples. N.T. and R.J.W. provided the fiber cavity mirror. S.G. and T.Z. wrote the manuscript with input from other authors. T.Z. developed the project and supervised the work.

Competing interests

The authors declare no competing interests.

Additional information

Supplementary information The online version contains supplementary material available at https://doi.org/10.1038/s41467-025-64780-6.

Correspondence and requests for materials should be addressed to Tian Zhong.

Peer review information *Nature Communications* thanks Gabriele de Boo and the other anonymous reviewers for their contribution to the peer review of this work. A peer review file is available.